Biophysical Journal, Volume *116*

Supplemental Information

The Effect of Cortical Elasticity and Active Tension on Cell Adhesion Mechanics

Bart Smeets, Maxim Cuvelier, Jiri Pešek, and Herman Ramon

The effect of cortical elasticity and active tension on cell adhesion mechanics
Supplementary Information

B. Smeets, M. Cuvelier, J. Pešek, H. Ramon

KU Leuven – MeBioS, Kasteelpark Arenberg 30, 3001 Heverlee, Belgium

1 Computational Method

Contact Mechanics In our numerical model, we represent deformable cells as triangulated meshes, where the local curvature is taken into account for each triangle by means of an encompassing sphere. The contact between two rounded triangles can be modeled by using the Maugis-Dugdale (MD) theory for overlapping spheres (1).

MD expands upon Hertz' pure repulsive contact model by taking into account the adhesive pressure associated with intimate contact between adherent surfaces – see Fig. S1. The MD contact pressure between two curved asperities A and B is given by the sum of Hertz and adhesive pressures:

$$p(r) = p_a(r) + p_H(r). \tag{S1}$$

The repulsive Hertz pressure acting on the contact area with radius a, for a given distance r from the center of the contact circle, is given by

$$p_H(r) = \frac{2\hat{E}_{AB}}{\pi \hat{R}_{AB}} \sqrt{a^2 - r^2}, \tag{S2}$$

with effective Young's modulus $\hat{E}_{AB}$ and contact radius $\hat{R}_{AB}$

$$\hat{E}_{AB} = \left(\frac{1-\nu_A^2}{E_A} + \frac{1-\nu_B^2}{E_B} \right)^{-1},$$

$$\hat{R}_{AB} = \left(\kappa_A + \kappa_B \right)^{-1},$$

where E_A, ν_A and κ_A refer to the Young's modulus, Poisson ratio and local curvature of a given asperity A. Adhesive stress is given by

$$p_a(r) = \begin{cases} -\frac{\sigma_0}{\pi} \arccos\left(\frac{2a^2 - c^2 - r^2}{c^2 - r^2} \right) & 0 < r < a, \\ -\sigma_0, & a < r < c, \end{cases} \tag{S3}$$

Here, σ_0 represents the maximal adhesive traction, which is related to the adhesion energy w as (3):

$$w = h_0 \, \sigma_0, \tag{S4}$$

where h_0 represents the maximum separation between the asperities beyond which the adhesive traction drops to zero.

Numerical integration of the contact pressures allows us to determine the net contact force and moment acting on a pair of triangles $(\alpha\beta)$. Assuming that the nodal contact forces $F_i^{\alpha\beta}$ must be colinear with the contact unit normal $\hat{\boldsymbol{n}}_{\alpha\beta}$, the system of linear equations per contact pair $(\alpha\beta)$:

$$\sum_{i \in \alpha} \boldsymbol{F}_i^{\alpha\beta} = - \sum_{q \in \alpha \cap \beta} A_q \, p(\|\boldsymbol{r}_q\|) \hat{\boldsymbol{n}}_{\alpha\beta}, \tag{S5}$$

$$\sum_{i \in \alpha} \left[\boldsymbol{x}_i - \boldsymbol{x}_C^{\alpha\beta} + \left[(\boldsymbol{x}_C^{\alpha\beta} - \boldsymbol{x}_i) \cdot \hat{\boldsymbol{n}}_{\alpha\beta} \right] \hat{\boldsymbol{n}}_{\alpha\beta} \right] \times \boldsymbol{F}_i^{\alpha\beta} = - \sum_{q \in \alpha \cap \beta} A_q p(\|\boldsymbol{r}_q\|) \boldsymbol{r}_q \times \hat{\boldsymbol{n}}_{\alpha\beta}, \tag{S6}$$

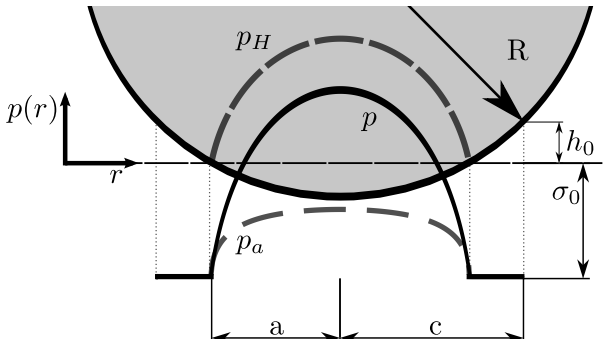

Figure S1: Illustration of contact between an asperity with radius R and a flat half-space. The total contact pressure p is the sum of the repulsive Hertz pressure p_H, acting within contact radius a and an adhesive Dugdale traction p_a, acting within contact radius c. For $a \leq r \leq c$, the adhesive traction is at its maximal value σ_0.

results in a unique solution for every $\boldsymbol{F}_i^{\alpha\beta}$. A_q is the weighted area associated with quadrature points q, covering the intersection polygon $\alpha \cap \beta$. $\boldsymbol{r}_q$ is the vector from the sphere-sphere[1] contact point $\boldsymbol{x}_C^{\alpha\beta}$ to the quadrature point. The solution for this system is presented in Odenthal et al. (1).

Cortex Elasticity Assuming small deformations, we use the Van Gelder model to approximate in-plane elastic behavior of the cortex using linear springs (4):

$$\boldsymbol{F}_{ij}^s = k_s(d_{ij} - d_{ij}^*)\hat{\boldsymbol{n}}_{ij}, \tag{S7}$$

with

$$\hat{\boldsymbol{n}}_{ij} = \frac{\boldsymbol{x}_j - \boldsymbol{x}_i}{\|\boldsymbol{x}_j - \boldsymbol{x}_i\|}, .$$

Here, $d_{ij} = \|\boldsymbol{x}_j - \boldsymbol{x}_i\|$ is the current distance and d_{ij}^* the resting distance between nodes i and j with positions $\boldsymbol{x}_i$ and $\boldsymbol{x}_j$. The linear spring stiffness k_s, under our assumption of an isotropic linear elastic material model, can be expressed as a function of E_c and t_c using Van Gelder's formula (4):

$$k_s = \frac{E_c t_c \left(A_{ij}^{\alpha} + A_{ij}^{\beta}\right)}{{d_{ij}^*}^2}, \tag{S8}$$

in which $A_{ij}^{\alpha} + A_{ij}^{\beta}$ is the area of the connected triangle pair $\alpha\beta$ – see Fig. S2(a). By using this expression we have implicitly assumed that the Poisson ratio is equal to $1/3$ (6). Due to its non-zero thickness, the cortex also has bending rigidity. The energy required to bend two connected triangles $(\alpha\beta)$ is given by

$$E_{\alpha\beta}^b = k_b\left(1 - \cos\left(\theta - \theta^*\right)\right), \tag{S9}$$

where θ^* and θ represent the spontaneous and instantaneous angles between a pair of adjacent triangles.

As with k_s, bending rigidity k_b can be estimated based on cortex properties to match to macroscopic (continuum) models. Based on the model of Helfrich (5)

$$k_b = \frac{E_c t_c^3}{12\left(1 - \nu_c^2\right)}, \tag{S10}$$

with ν_c Poisson's ratio of the cortex. To be consistent with the assumption of an isotropic linear elastic material, ν_c is fixed at a value of $1/3$ (6), hence $k_b = 3E_c\, t_c^3/32$. For a pair of connected triangles $\alpha\beta$, the bending moment is:

$$\boldsymbol{M}_{\alpha\beta}^b = -k_b(\theta - \theta^*)\frac{\boldsymbol{x}_{\alpha\beta}^{c2} - \boldsymbol{x}_{\alpha\beta}^{c1}}{\left\|\boldsymbol{x}_{\alpha\beta}^{c2} - \boldsymbol{x}_{\alpha\beta}^{c1}\right\|}, \tag{S11}$$

for small angle deviations when $\sin\left(\theta - \theta^*\right) \approx \theta - \theta^*$, and with $\boldsymbol{x}_{\alpha\beta}^{c1}$ and $\boldsymbol{x}_{\alpha\beta}^{c2}$ the positions of the connected triangles' common nodes, sorted counter-clockwise with respect to the triangle normal vectors $\hat{\boldsymbol{n}}_\alpha$ and $\hat{\boldsymbol{n}}_\beta$ – see Fig. S2(b). This couple

[1] Each triangle with curvature κ can be associated with a unique sphere with radius $1/\kappa$, see (1).

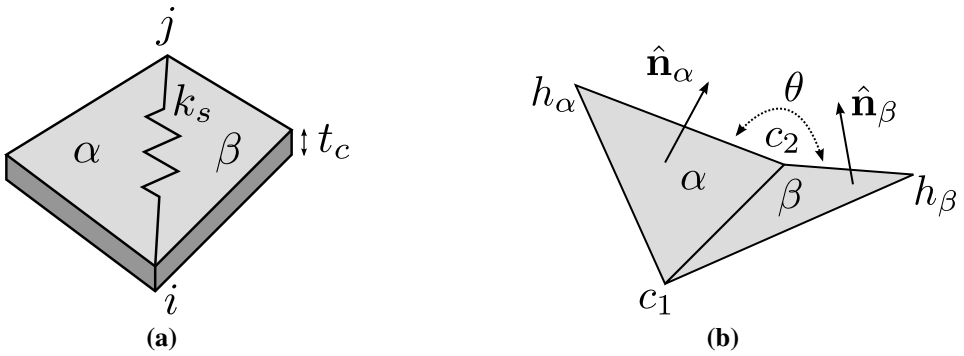

Figure S2: **(a)**: Illustration of elementary spring element between nodes i and j. The spring constant k_s is based on a thin shell element containing adjacent triangles α and β, and with thickness t_c – Eq. (S8). **(b)**: Illustration of two connected triangles α and β with normal unit vectors $\hat{\boldsymbol{n}}_\alpha$ and $\hat{\boldsymbol{n}}_\beta$ between whom a bending moment is computed based on the instantaneous angle θ. Furthermore, we have indicated (sorted) common nodes c_1 and c_2 and lever nodes h_α and h_β.

is translated to mechanically equivalent forces on the four nodes of the triangle pair. For each triangle, the sum of all three forces must be zero, and the generated moment w.r.t. the common axis must be $\boldsymbol{M}^b_{\alpha\beta}$. These conditions lead to following unique total nodal forces:

$$\boldsymbol{F}^{h_\alpha}_{\alpha\beta} = -\boldsymbol{M}^b_{\alpha\beta} \times \boldsymbol{h}_\alpha, \tag{S12}$$

$$\boldsymbol{F}^{h_\beta}_{\alpha\beta} = \boldsymbol{M}^b_{\alpha\beta} \times \boldsymbol{h}_\beta, \tag{S13}$$

$$\boldsymbol{F}^{c1}_{\alpha\beta} = \frac{y^{c2}_\beta}{y^{c1}_\beta - y^{c2}_\beta}\left(\boldsymbol{M}^b_{\alpha\beta} \times \boldsymbol{h}_\beta\right) - \frac{y^{c2}_\alpha}{y^{c1}_\alpha - y^{c2}_\alpha}\left(\boldsymbol{M}^b_{\alpha\beta} \times \boldsymbol{h}_\alpha\right), \tag{S14}$$

$$\boldsymbol{F}^{c2}_{\alpha\beta} = \frac{y^{c1}_\beta}{y^{c2}_\beta - y^{c1}_\beta}\left(\boldsymbol{M}^b_{\alpha\beta} \times \boldsymbol{h}_\beta\right) - \frac{y^{c1}_\alpha}{y^{c2}_\alpha - y^{c1}_\alpha}\left(\boldsymbol{M}^b_{\alpha\beta} \times \boldsymbol{h}_\alpha\right). \tag{S15}$$

h_α and h_β indicate the indices of the (non-common) "lever" node of triangles α and β. $\boldsymbol{h}_\alpha$ and $\boldsymbol{h}_\beta$ are the orthogonal height vectors from the common axis to lever nodes h_α and h_β. Finally,

$$y^{cj}_k = (\boldsymbol{x}^{cj}_{\alpha\beta} - \boldsymbol{x}^{h_k}_{\alpha\beta}) \cdot (\boldsymbol{x}^{c2}_{\alpha\beta} - \boldsymbol{x}^{c1}_{\alpha\beta}), \tag{S16}$$

for $k \in [\alpha, \beta]$ and $j \in [1, 2]$.

Active cortical tension Tension generated in the cortex results form myosin contractility which can be be interpreted as an effective surface tension γ in the cortical shell model. γ helps in maintaining cell shape and decreases the local curvature on longer time-scales. Based on the Young-Laplace law, the pressure contribution due to γ is given by

$$P^\gamma_i = -2\gamma\kappa_i, \tag{S17}$$

with κ_i being the local curvature. Active volume control also contributes to the cytoplasmic pressure. As the equilibrium volume of a cell is assumed to be constant at short time-scales, an effective bulk modulus K is introduced. The cytoplasmic pressure due to volume control P^v can thus be estimated as

$$P^v = -K\frac{V - V^*}{V^*}. \tag{S18}$$

V^* and V represent the spontaneous and instantaneous volume of the cell. The resulting nodal force due to the total internal pressure P is given by

$$\boldsymbol{F}^p_i = \hat{\boldsymbol{n}}_i \mathcal{A}_i P_i = \hat{\boldsymbol{n}}_i \mathcal{A}_i \left(P^\gamma_i + P^o + P^v\right), \tag{S19}$$

with $\mathcal{A}_i$ and $\hat{\boldsymbol{n}}_i$ the Voronoi area (1) and normal associated with a given node. Moreover, we assume that a constant (e.g. osmotic) pressure $P^o = 2\gamma/R$ exists that ensures that the free cell is mechanically at rest.

Dissipative forces Our method is based on solving overdamped equations of motion. Hence, dissipative forces are required to balance these equations of motion. The general methodology tries to introduce these dissipative forces in a consistent manner in terms of viscosities of modeled materials. A general drag force $\boldsymbol{F}_i^l$ is included to account for the liquid drag between the cells and their medium:

$$\boldsymbol{F}_i^l = -\lambda_l \mathcal{A}_i \boldsymbol{v}_i, \tag{S20}$$

with $\mathcal{A}_i$ the Voronoi area of node i. For spherical cells with radius R

$$\lambda_l = \frac{3\eta_l}{2R} \tag{S21}$$

can be used to estimate λ_l, introducing fluid viscosity η_l. When dealing with arbitrary shapes this approximation is no longer correct and we would in principle require the microscopic resolution of the fluid flow field in and around the cell surface. However, as F_i^d is typically very small compared to other dissipative forces at the seconds/minutes timescale, this approximation is sufficient. Likewise, we can increase the fluid viscosity above realistic values to dampen numerical oscillations without any influence on simulation results. A much larger contribution to energy dissipation arises from viscosity of the cortex itself. The viscous damping force between two connected nodes i and j is computed as

$$\boldsymbol{F}_{ij}^d = \Lambda_{ij}^d (\boldsymbol{v}_j - \boldsymbol{v}_i), \tag{S22}$$

with friction elements ($\boldsymbol{I}$ being identity)

$$\Lambda_{ij}^d = \frac{t_c\, \eta_c}{\sqrt{3}}\, \boldsymbol{I}.$$

where the $1/\sqrt{3}$ factor accounts for the triangular connectivity of the shell. Finally, a viscous contact force is included to account for drag between contacting triangles. The contact drag force acting on node i of triangle α of the contacting pair $(\alpha\beta)$

$$\boldsymbol{F}_{\alpha\beta,i}^c = \Lambda_{\alpha\beta}^c \cdot \sum_{\forall k \in \beta} w_{\alpha\beta,ik}\, (\boldsymbol{v}_k - \boldsymbol{v}_i), \tag{S23}$$

again, determined by a friction tensor $\Lambda_{\alpha\beta}^c$ and weights $w_{\alpha\beta,ik}$ per node k of the β triangle. $w_{\alpha\beta,ik}$ are assumed to scale with the relative contribution of the nodal contact forces to the overall contact force, thus

$$w_{\alpha\beta,ik} = \frac{(\boldsymbol{F}_{\alpha\beta,i} + \boldsymbol{F}_{\alpha\beta,k}) \cdot \hat{\boldsymbol{n}}_{\alpha\beta}}{6 \sum\limits_{\forall k \in \beta} \boldsymbol{F}_{\alpha\beta,k}^{MD} \cdot \hat{\boldsymbol{n}}_{\alpha\beta}}, \tag{S24}$$

$\Lambda_{\alpha\beta}^c$ for a given contact area $A_{\alpha\beta}^c$ between triangles α and β is estimated as:

$$\Lambda_{\alpha\beta}^c = A_{\alpha\beta}^c \left[\lambda_n \hat{\boldsymbol{n}}_{\alpha\beta} \cdot \hat{\boldsymbol{n}}_{\alpha\beta}^T + \lambda_t \left(\boldsymbol{I} - \hat{\boldsymbol{n}}_{\alpha\beta} \cdot \hat{\boldsymbol{n}}_{\alpha\beta}^T \right) \right], \tag{S25}$$

with normal and tangential friction coefficients[2] λ_n and λ_t.

Equation of motion Neglecting inertial contributions for the overdamped cellular system, the complete force balance for node i can be expressed based on the different contributions described above

$$\begin{aligned} &\sum_{\text{con.}j} \boldsymbol{F}_{ij}^s + \sum_{(\alpha\beta):i\in\alpha} \boldsymbol{F}_i^{\alpha\beta} + \sum_{(\alpha\beta):i\in\alpha} \boldsymbol{F}_{\alpha\beta,i}^b + \boldsymbol{F}_i^p \\ &= \\ &\sum_{\text{con.}j} \Lambda_{ij}^d \cdot w_{ij}\, (\boldsymbol{v}_i - \boldsymbol{v}_j) + \sum_{(\alpha\beta):i\in\alpha} \left[\Lambda_{\alpha\beta,i}^c \cdot \sum_{\forall k \in \beta} w_{\alpha\beta,ik}\, (\boldsymbol{v}_i - \boldsymbol{v}_k) \right] + \lambda^l \mathcal{A}_i \boldsymbol{v}_i, \end{aligned} \tag{S26}$$

For a system of N nodes, Eq. (S26) can be summarized as:

$$\underline{\boldsymbol{F}} = \underline{\Lambda} \cdot \underline{\boldsymbol{v}}, \tag{S27}$$

[2]Note that the units of friction coefficient λ_n and λ_t are Pa·s/m, as they relate a velocity difference between two contacting surface to a dissipative contact stress.

which consist of a $(3N \times 1)$, $(3N \times 3N)$ and $(3N \times 1)$ matrix for three-dimensional systems. $\underline{\Lambda}$ is a symmetric and positive definite matrix

$$\underline{\Lambda} = \sum_{i,j \in N} \begin{pmatrix} 0 & \cdots & & & \\ \cdots & \Lambda_{ij} & \cdots & -\Lambda_{ij} & \cdots \\ \vdots & \vdots & \ddots & \vdots & \\ \cdots & -\Lambda_{ij} & \cdots & \Lambda_{ij} & \cdots \\ & & & \cdots & 0 \end{pmatrix} + \begin{pmatrix} \lambda_l & 0 & \cdots & & \\ 0 & \lambda_l & 0 & \cdots & \\ \vdots & & \ddots & & \vdots \\ & & 0 & \lambda_l & 0 \\ 0 & & \cdots & 0 & \lambda_l \end{pmatrix}, \tag{S28}$$

where Λ_{ij} are (3×3) matrices created by $w_{ij}\Lambda^d_{ij} + w_{\alpha\beta,ij}\Lambda^c_{\alpha\beta_i}$. Since $\underline{\Lambda}$ is extremely sparse and always positive definite (1, 9), the conjugate gradient method can be used to efficiently solve the system for nodal velocities $\underline{\boldsymbol{v}}(t)$ at each time increment. The positions of the nodes $\underline{\boldsymbol{x}}$ are subsequently updated using a forward Euler scheme:

$$\underline{\boldsymbol{x}}(t + \Delta t) = \underline{\boldsymbol{x}}(t) + \Delta t\, \underline{\boldsymbol{v}}(t). \tag{S29}$$

Implementation The computational model was implemented in the C++ particle-based simulation framework '*Mpacts*'. The deformable cell model was first introduced in (1), and later expaned upon for shell mechanics in (2). For solving over-damped systems, we use a semi-implicit method – see Eq. (S27), where a friction matrix is assembled that contains contact friction (or stiffness) elements. Each timestep, this linear system is iteratively solved using the Conjugate Gradient implementation of the C++ linear algebra library Eigen (10) which is optimized for vectorization and performance. Furthermore, a multi-grid contact detection scheme (11) was used to efficiently resolve pairs of contacting triangles between the contact pressures described above were numerically integrated. Numerical integration was performed using a 7-point symmetric Gaussian quadrature rule as derived in (12). Highly regular triangulated surface meshes of spherical cells were obtained by the progressive subdivision of an icosahedron – see e.g. (1). We used 5-level subdivisions (resulting in 2562 vertices and 5120 triangles) for the results in Fig. 3 and Fig. 4 and 6-level subdivisions (resulting in 10242 vertices and 20480 triangles) for the results in Fig. 6, where a greater refinement was adopted for the estimates of contact radius.

2 Simulation setup

Here, we summarize the technical aspects of the performed simulations. In this work, we have considered four distinct setups: MA, DPA, optical tweezers and, very briefly, compression between two parallel plates.

Table S1: Complete list of parameters used to simulate the MA experiments shown in Fig. 4(b). Square brackets indicate ranges of parameters that were varied across multiple simulations.

Parameter	**Symbol**	**Value(s)**	**Units**
Young's modulus cortex	E_c	[5, 35]	kPa
Poisson's ratio cortex	ν_c	1/3	-
Thickness cortex	t_c	[0.15, 0.65]	μm
Viscosity cortex	η_c	0.5	kPa·s
Active tension cortex	γ	[0, 0.9]	nN/μm
Bulk modulus cell	K	25	kPa
Liquid viscosity	η_l	5.0	Pa·s
Normal cell-pipette friction	λ^p_n	5.0	kPa·s/μm
Tangential cell-pipette friction	λ^p_t	0.1	kPa·s/μm
Cell radius	R	6	μm
Simulation timestep	Δt	0.75	ms
Maximal error conjugate gradient	F_{res}	1.0	pN
Number of mesh nodes per cell	N_v	2562	-
Pipette inner radius	R_p	3.5	μm
Pipette rounding radius	R_r	0.5	μm
Pipette stiffness	k_p	40	kPa·s/μm
Pressure increase rate	$\mathrm{d}\Delta P/\mathrm{d}t$	25	Pa/s

Micropipette Aspiration The micropipette is represented as a hollow cylinder, with a torus glued at the end, with a tube (rounding) radius $R_r = 0.5\,\mu\mathrm{m}$, and an inner radius (equal to the cylinder radius) of $R_p = 3.5\,\mu\mathrm{m}$ – see Fig. 2(a). An underpressure ΔP is applied on any node of the deformable cell that has crossed the center of the pipette's bounding torus. The aspiration force on the node is simply:

$$\boldsymbol{F}_i^{p,a} = \mathcal{A}_i \Delta P\, \hat{\boldsymbol{n}}_i, \tag{S30}$$

with $\mathcal{A}_i$ and $\hat{\boldsymbol{n}}_i$ the Voronoi area and normal associated with node i. Overlap with the pipette wall is prevented using a linear stiffness k_p. The contact force on the node is:

$$\boldsymbol{F}_i^{p,c} = k_p\, \mathcal{A}_i \delta_i^p\, \hat{\boldsymbol{n}}_c(\boldsymbol{x}_i), \tag{S31}$$

if overlap distance $\delta_i^p > 0$ and zero otherwise. $\hat{\boldsymbol{n}}_c(\boldsymbol{x}_i)$ is the normal direction of the pipette's inner surface at the position of node i. Both δ_i^p and $\hat{\boldsymbol{n}}_c$ can be trivially obtained from simple geometric considerations. We set $k_p = 40\,\mathrm{kPa}/\mu\mathrm{m}$, sufficiently high to prevent any meaningful overlap in the range of applied pressure. For nodes that are in contact with the pipette ($\delta_i^p > 0$), we include an additional contact drag force:

$$\boldsymbol{F}_i^{p,d} = -\Lambda_i^p\, \boldsymbol{v}_i, \tag{S32}$$

with friction tensor

$$\Lambda_i^p = \mathcal{A}_i \left[\lambda_n^p \hat{\boldsymbol{n}}_{ij} \hat{\boldsymbol{n}}_{ij}^T + \lambda_t^p \left(I - \hat{\boldsymbol{n}}_{ij} \hat{\boldsymbol{n}}_{ij}^T \right) \right],$$

where λ_n^p and λ_t^p are normal and tangential cell-pipette friction constants. We set $\lambda_n^p = 5\,\mathrm{kPas}/\mu\mathrm{m}$, sufficiently high to dampen numerical oscillations in the stiff potential k_p and $\lambda_t^p = 0.1\,\mathrm{kPas}/\mu\mathrm{m}$, sufficiently low to represent quasi-frictionless contact.

In the MA simulation, we start at $\Delta P = 0\,\mathrm{Pa}$, and gradually increase ΔP until the aspirated length $L_p = R_p$, i.e. the aspirated region forms a hemisphere in the micropipette. The current pressure at this point is registered as the critical pressure P_c. The rate of pressure increase must be sufficiently slow with respect to the viscous relaxation time of the cell. We set $\mathrm{d}\Delta P/\mathrm{d}t = 25\,\mathrm{Pa/s}$. The full set of parameters used to perform the MA simulations is listed in Table S1.

Dual Pipette Aspiration The DPA simulation consists of two subsequent steps: 1) Two cells are put in close proximity[3] and allowed to freely adhere until they equilibrate at a stable contact area and 2) We apply opposite pulling forces on both cells and register their separation. Hence, we do not represent the two micropipettes explicitly, but simply distribute a pulling force over the cell. To do this, we adopt two configurations:

A For the results in Fig. 3 and Fig. 4, we distribute the total force evenly over all nodes with a contact area equal to zero. Such a distribution is numerically more favorable, since it ensures a low excess force for each degree of freedom. In these simulations, we were only interested in the pull-off force, which was verified to be affected very little by the precise manner of force distribution.

B For Fig. 6, we must quantify the shape (R_a) and the geometry of the contact area (R_c). In order to compare to (7), we need to adopt their assumptions, which include that the pulling force is applied only at the top of the cell. Here, we selected the top 5% of mesh nodes at either side of the cell doublet, and distributed the pulling force evenly among them.

The purpose of configuration A is to measure the pull-off force. For this, we very slowly increase the applied force applied to the cells, and register the force at which rapid detachment of the cell-cell contact occurs. Using this setup, we can accurately quantify the pull-off force in one simulation, as long as the rate of applied force increase is much slower than the relaxation dynamics of the cell. We set $\mathrm{d}F/\mathrm{d}t = 0.25\,\mathrm{nN/s}$.

For configuration B, we perform a separate and independent simulation for each applied force F. To ensure that a stable configuration is reached, we simulate until either the two cells have been fully separated, or until a pulling time of $60\,\mathrm{s}$ has passed. After this, the current contact area A_c between the two cells is registered, and a corresponding contact radius $R_c = \sqrt{A_c/\pi}$. To obtain a robust estimate of the apical radius R_a, we follow the following procedure:

I Obtain the contact axis $\hat{\boldsymbol{n}}_{AB}$ for cells A and B as:

$$\hat{\boldsymbol{n}}_{cc} = \frac{1}{A_{c,A} + A_{c,B}} \left(\sum_{\forall i \in A} A_{c,i} \hat{\boldsymbol{n}}_i - \sum_{\forall i \in B} A_{c,i} \hat{\boldsymbol{n}}_i \right),$$

where $A_{c,i}$ is the contact area and $\hat{\boldsymbol{n}}_i$ the surface normal vector of node with index i.

[3] The cells must be at least within their adhesive range h_0 so that the adhesion process may start.

Table S2: Complete list of parameters used to simulate the DPA experiments in shown in Fig. 3. Square brackets indicate ranges of parameters that were varied across multiple simulations.

Parameter	**Symbol**	**Value(s)**	**Units**
Young's modulus cortex	E_c	30	kPa
Normal contact stiffness	$E_{c,c}$	30	kPa
Poisson's ratio cortex	ν_c	1/3	-
Thickness cortex	t_c	[0.15, 2.5]	µm
Viscosity cortex	η_c	2.67	kPa·s
Active tension cortex	γ	[0, 1.5]	nN/µm
Bulk modulus cell	K	30	kPa
Liquid viscosity	η_l	1.0	Pa·s
Normal cell-cell friction	λ_n	0.05	kPa·s/µm
Tangential cell-cell friction	λ_t	0.05	kPa·s/µm
Cell-cell adhesion	w	0.25	nN/µm
Effective range of adhesion	h_0	50	nm
Cell radius	R	10	µm
Simulation timestep	Δt	0.5	ms
Maximal error conjugate gradient	F_{res}	5.0	pN
Number of mesh nodes per cell	N_v	2562	-
Rate of force increase	$\mathrm{d}F/\mathrm{d}t$	0.25	nN/s

Table S3: Complete list of parameters used to simulate the DPA experiments shown in Fig. 4 and Fig. 6. Square brackets indicate ranges of parameters that were varied across multiple simulations.

Parameter	**Symbol**	**Value(s)**	**Units**
Young's modulus cortex	E_c	[5, 35]	kPa
Normal contact stiffness	$E_{c,c}$	100	kPa
Poisson's ratio cortex	ν_c	1/3	-
Thickness cortex	t_c	[0.15, 0.65]	µm
Viscosity cortex	η_c	2.67	kPa·s
Active tension cortex	γ	[0, 0.9]	nN/µm
Bulk modulus cell	K	30	kPa
Liquid viscosity	η_l	1.0	Pa·s
Normal cell-cell friction	λ_n	0.05	kPa·s/µm
Tangential cell-cell friction	λ_t	0.05	kPa·s/µm
Cell-cell adhesion	w	[0.05, 0.9]	nN/µm
Effective range of adhesion	h_0	50	nm
Cell radius	R	6	µm
Simulation timestep	Δt	1.0	ms
Maximal error conjugate gradient	F_{res}	5.0	pN
Number of mesh nodes per cell	N_v	[2562, 10242]	-

II Obtain the center of the contact $\boldsymbol{x}_{cc}$ by integrating:

$$\boldsymbol{x}_{cc} = \frac{1}{A_{c,A} + A_{c,B}} \left(\sum_{\forall i \in A} A_{c,i} \hat{\boldsymbol{x}}_i - \sum_{\forall i \in B} A_{c,i} \hat{\boldsymbol{x}}_i \right).$$

III For each node i, compute the distance r_i to the line defined by $\boldsymbol{x}_{cc}$ and $\hat{\boldsymbol{n}}_{cc}$.

IV For each node i, compute the (positive) distance x_i along the line defined by $\boldsymbol{x}_{cc}$ and $\hat{\boldsymbol{n}}_{cc}$.

V Sort each node i in one of 25 bins along the central axis according to x_i.

VI Compute the average radius r_i for each bin k:

$$r_k = \frac{1}{N_k} \sum_{\forall i \in k} r_i.$$

Table S4: Complete list of simulation parameters used to simulate the optical trap experiments shown in Fig. 5.

Parameter	**Symbol**	**Value(s)**	**Units**
Young's modulus cortex	E_c	15	kPa
Normal contact stiffness	$E_{c,c}$	100	kPa
Poisson's ratio cortex	ν_c	1/3	-
Thickness cortex	t_c	0.3	µm
Viscosity cortex	η_c	2.67	kPa·s
Active tension cortex	γ	0.4	nN/µm
Bulk modulus cell	K	30	kPa
Liquid viscosity	η_l	1.0	Pa·s
Normal cell-substrate friction	$\lambda_{n,s}$	0.15	kPa·s/µm
Tangential cell-substrate friction	$\lambda_{t,s}$	0.15	kPa·s/µm
Tangential cell-bead friction	$\lambda_{t,b}$	0.20	kPa·s/µm
Tangential cell-bead friction	$\lambda_{t,b}$	0.20	kPa·s/µm
Cell-bead adhesion	w	0.517	nN/µm
Effective range of adhesion	h_0	50	nm
Cell radius	R	7	µm
Patch size	L_p	10	µm
Bead radius	R_b	1.8	µm
Simulation timestep	Δt	2.0	ms
Maximal error conjugate gradient	F_{res}	5.0	pN
Number of mesh nodes per cell	N_v	10242	-

VII The maximal r_k is recorded as the apical radius: $R_a = \max(r_k)$

Fig. S3 illustrates this procedure for a specific cell configuration. The maximum of the black line gives the apical radius R_a.

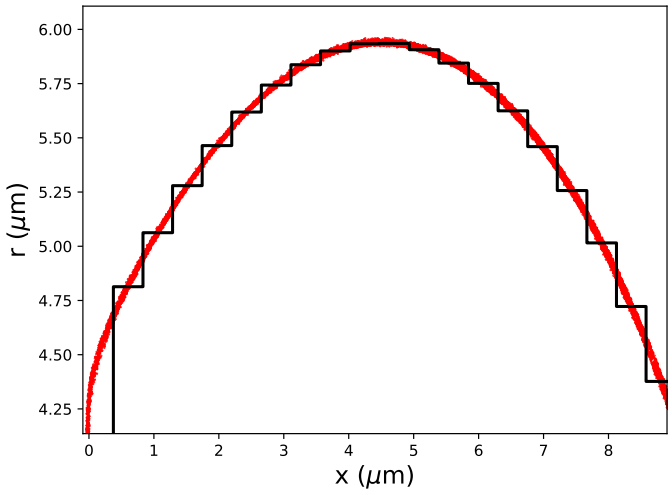

Figure S3: Illustration of algorithm to robustly compute the apex radius R_a: node positions (red dots) are collected in axial bins, based on the distance to the contact plane. For each axial bin (25 in total), the average distance to the axis is computed. The maximal of these values gives the apical radius R_a. In the shown configuration, we can estimate $R_a \approx 5.9\,\mu\text{m}$.

Optical tweezers To replicate an optical tweezers experiment in a simulation, we create a surface for the cell to spread on which is composed of two 'patches'. A central, rectangular patch of $10\,\mu\text{m} \times 10\,\mu\text{m}$ (indicated in green in Fig. 5) has a very high adhesion energy, while the surrounding patch (indicated in black in Fig. 5) has no adhesion. We set the adhesion energy between cell and substrate $w_{c,s}$ to $0.8\,\text{nN}/\mu\text{m}$, sufficiently high to ensure that the full patch will be covered by the cell. The cell radius was slightly increased (from $6\,\mu\text{m}$ to $7\,\mu\text{m}$) to be consistent with the results shown in (8). Next, we let the cell adhere to the surface until its positions equilibrate (Fig. 5 top left). In a second phase, we relax all elastic stresses (assuming

that the spreading could occur over a long timescale), and let a bead adhere to the side of the cell, at the height where it maximally protrudes. The adhesion energy between cell and bead $w_{c,b}$ is tuned so that the experimentally observed contact radius is approximated. Finally, we apply various pulling forces to the bead and record the displacement of the bead. Each simulation is repeated for 5 random orientations of the cell (to artifacts due to mesh coarseness near the cell-bead contact area). The slope of displacement with respect to pulling force is used to estimate an apparent Young's modulus of the cell. The full Table of simulation parameter used for this experimental setup is shown in Table S4.

Parameter choice As mentioned in 'Computational Model', a requirement for the applied contact model to be valid is that the normal elastic compression is sufficiently small compared to the cortex thickness. For Fig. 3, we have ensured this by choosing a sufficiently high E_c and a sufficiently low w when varying the thickness t_c over a wide range (parameters listed in Table S2). On the other hand, for our estimated parameters of the S180 cell, the elastic modulus of the cortex is relatively low ($\approx$ 15 kPa) and the thickness is very small ($\approx$ 0.3 μm). In this case, when adhesion w is high, the Hertzian assumptions are violated. However, in these cases the normal elastic compression (which is always $\ll t_c$), is negligible compared to the total deformation of the cell. Thus, we can safely and without loss of accuracy increase the effective stiffness of the contact model $E_{c,c} > E_c$, so that large and incorrectly computed overlap distances are prevented. The full set of parameters to simulate these configurations is listed in Table S3. The sub-set of this table that contains our estimates for S180 cells was provided in Table 1.

Aside from the parameters that extensively discussed in the main manuscript (E_c, ν_c, t_c, γ), the numerical simulations require some additional parameters. Since we solve a dynamic system, the forces on the right hand side are balanced by viscosities / damping forces. These viscosities do not influence the steady-state results discussed in the main manuscript, but are required for the numerical convergence. The order of magnitude of these viscosities is chosen in the range of estimates for real biological cells (i.e. kPa·s/μm for cell-cell frictions and kPa·s for cortex viscosity (13)). The simulation time step is varied based on the specific simulation setup (from $0.5\,\mathrm{ms}$ to $2\,\mathrm{ms}$). The Conjugate Gradient solver was assigned the convergence criterion of a maximal force residual of 5 pN.

References

1. Odenthal T, et al. (2013) Analysis of initial cell spreading using mechanistic contact formulations for a deformable cell model. *PloS Comp Biol* 9(10): e1003267.
2. Guyot Y, et al. (2016). Immersed Boundary Models for Quantifying Flow-Induced Mechanical Stimuli on Stem Cells Seeded on 3D Scaffolds in Perfusion Bioreactors. *PLoS Comp Biol* 12(9) e1005108.
3. Johnson KL, Greenwood JA (1997) An adhesion map for the contact of elastic spheres. *J. Colloid Interface Sci* 192(2): 326-333.
4. Van Gelder A (1998) Approximate Simulation of Elastic Membranes by Triangulated Spring Meshes. *Journal of Graphics Tools* 3(2): 21–41.
5. Helfrich W (1973) Elastic properties of lipid bilayers: theory and possible experiments. *Verlag der Zeitschrift für Naturforschung* 28(11-12): 693–703.
6. Kot M, Nagahashi H, Szymczak P (2015) Elastic moduli of simple mass spring models. *Visual Computer* 31(10): 1339–1350.
7. Brochard-Wyart F, de Gennes PG (2003) Unbinding of adhesive vesicles. *C.R. Phys* 4, 281.
8. Al Kilani A, et al. (2011) Negative Feedback from Integrins to Cadherins: A Micromechanical Study. *Biophys J* 101: 336 – 344.
9. Van Liedekerke P, et al. (2013) Solving microscopic flow problems using stokes equations in sph. *Comp Phys Comm* 184: 1686–1696.
10. Guennebaud G, Benoît J, et al. (2010) Eigen v3. *http://eigen.tuxfamily.org*.
11. He K, Dong S, and Zhou Z (2007). Multigrid contact detection method. *Physical Review E* 75(3): p.036710.
12. Dunavant DA (1985) High degree efficient symmetrical Gaussian quadrature rules for the triangle. *International Journal for Numerical Methods in Engineering* 21(6): 1129 – 1148.
13. Bausch AR, et al. (1998) Local Measurements of Viscoelastic Parameters of Adherent Cell Surfaces by Magnetic Bead Microrheometry. *Biophys J* 75: 2038 – 2049.
14. Seifert U, Lipowsky R (1995) Morphology of vesicles. *Handbook of biological physics* 1: 403 – 464.

3 Supplementary Figures

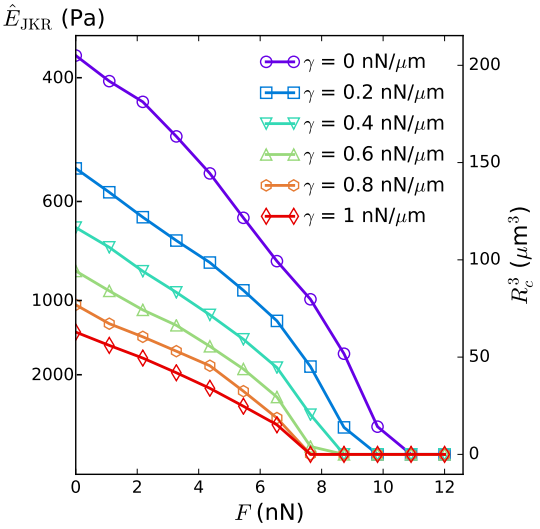

Figure S4: Cube of the contact radius R_c^3 as a function of pulling force F with varying active tension γ for cell mechanical properties in Table 1. The axis on the left hand side indicates the equivalent combined JKR modulus that yields the corresponding contact radius at zero loading ($F = 0$), computed using Eq. (5). Active tension has the effect of greatly increasing the apparent stiffness of the cell.

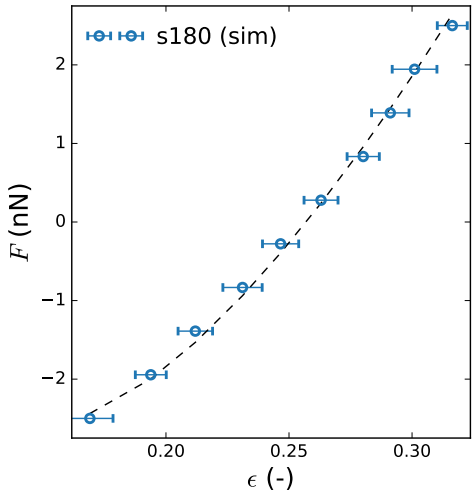

Figure S5: Simulation of cell compression between two rigid parallel plates. The cell has been assigned the parameters from Table S3, with $w = 0.3\,\mathrm{nN/\mu m}$ for both top and bottom plate and with $N_v = 2562$. Next, a compressive (positive) or tensile (negative) force F is applied on the top plate and the system is allowed to equilibrate. The final distance between the plates Δz is registered to compute the strain $\epsilon = (2R - \Delta z)/2R$, and this for five independent configurations, where we have rotated our initial mesh to random orientations, to prevent discretization artifact. The error bars show the standard deviation among these initial orientations. The dashed line shows a fit of $F \sim \epsilon^{3/2}$ to demonstrate the Hertzian response of the highly deformed cell.

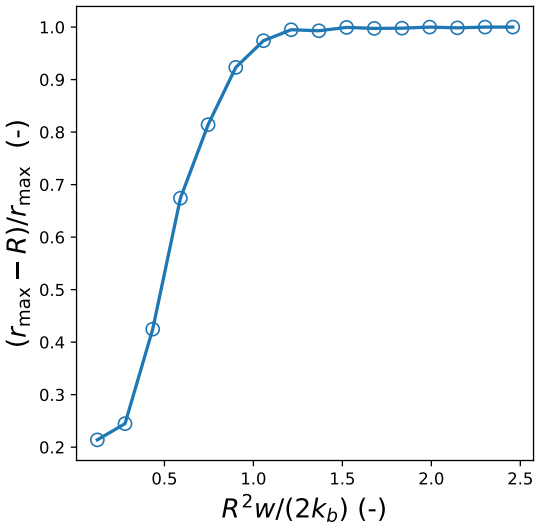

Figure S6: Comparison of deformable cell model cell spreading simulation with adhesion criterion $w = 2k_b/R^2$ for idealized vesicles (14). The limit of ideal vesicles (no volume change, no area change) is approached by setting $E_c = 100\,\mathrm{kPa}$, $t_c = 250\,\mathrm{nm}$ and $\gamma = 0\,\mathrm{nN/\mu m}$. This plot shows the degree of 'flatness' as a function of normalized adhesion energy with $r_{\max}$ the maximal radius of curvature. For $R^2w/(2k_b) < 1$, no flattened area is present because adhesion is insufficient to counteract the local bending resistance. Adhesion here only exists due to the finite adhesive range h_0. For $R^2w/(2k_b) > 1$, adhesion is able to overcome the bending resistance and establish a flattened contact area.

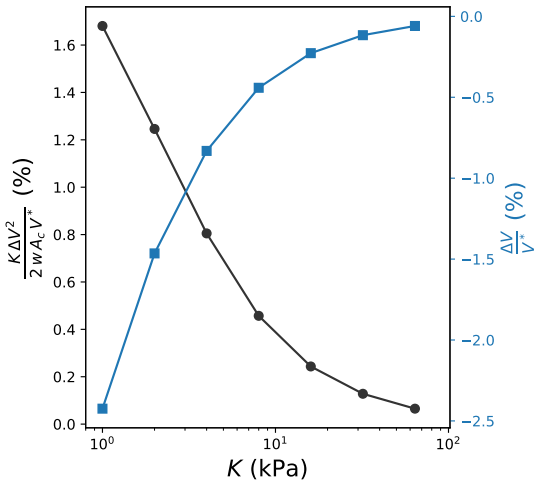

Figure S7: Influence of bulk modulus K in a simulated cell spreading experiment using parameters from Table 1. Black: Ratio of total hydrostatic energy $\frac{1}{2}K\Delta V^2/V^*$ and total adhesion energy $w\,A_c$ (contact area A_c) for varying cell bulk modulus K, using parameters from Table 1, and $w = 0.2\,\mathrm{nN/\mu m}$. The mechanical energy stored in hydrostatic compression decreases with increasing K, but its mechanical contribution relative to adhesion energy is small, even for small K. Blue: Relative change of the cells' volume for varying K.

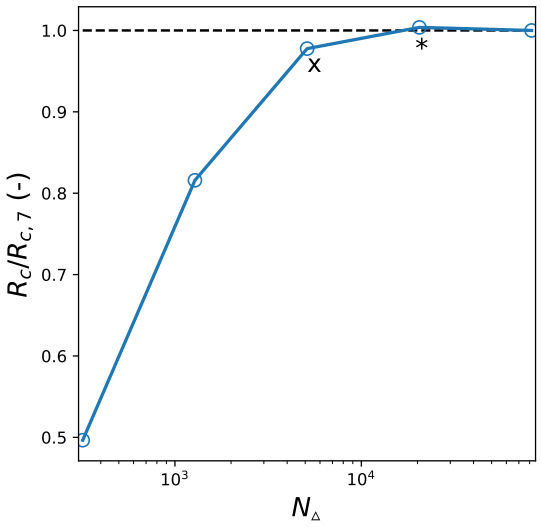

Figure S8: Contact radius as a function of number of triangles N_Δ of the triangulated mesh that represents the cell, for a cell spreading simulation with parameters from Table 1, and $w = 0.2\,\mathrm{nN/\mu m}$. The final contact radius R_c after cell spreading is shown relative to the contact radius of the most refined mesh $R_{c,7}$, which has 40,962 vertices and 81,920 triangles. The refinements used in this study are indicated with symbols: $N_\Delta^\times = 5{,}120$; $N_\Delta^* = 20{,}480$.

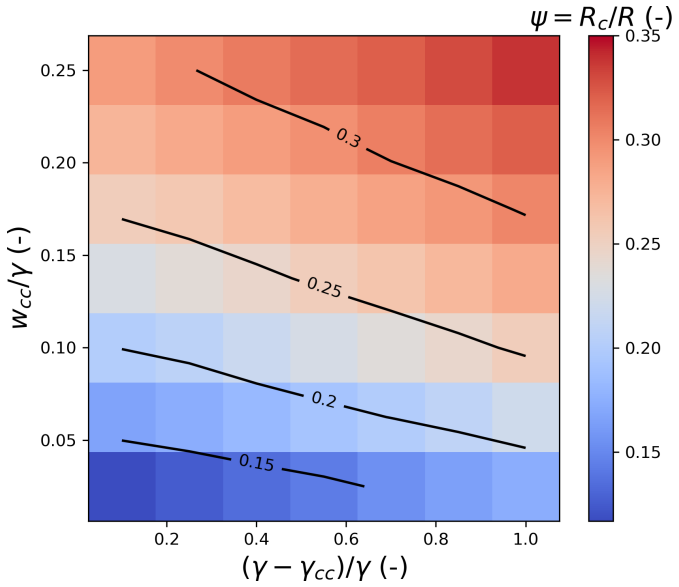

Figure S9: Relative contribution of cell-cell adhesion energy w_{cc} and differential interfacial tension $(\gamma - \gamma_{cc})/\gamma$ with γ_{cc} the active tension in the cell-cell contact region, to the radius of contact of an adhering cell doublet. Each 'pixel' represents an individual simulation with $E_c = 15\,\mathrm{kPa}$, $t_c = 0.3\,\mu\mathrm{m}$ $\gamma = 1.0\,\mathrm{nN/\mu m}$, where γ_{cc} and w_{cc} were varied as indicated.

Table S5: Summary of a linear model of relative contact area $\frac{A_c}{4\pi R^2} \sim a_0 + a_1 \frac{\gamma_{cc}}{\gamma} + a_2 \frac{w_{cc}}{\gamma}$ for a simulated cell-cell adhesion simulation (Fig. S9) with E_c =15 kPa, $t_c = 0.3\,\mu\text{m}$, $\gamma = 1.0\,\text{nN}/\mu\text{m}$, and varying cell-cell adhesion energy w_{cc} and cortical tension at the cell-cell interface γ_{cc}. Obtained parameter estimates are $a_0 = 0.0004 \pm 0.001$, $a_1 = 0.0275 \pm 0.001$ and $a_2 = 0.3449 \pm 0.005$ Data automatically generated by *statsmodels* in Python.

Dep. Variable:	contact area	**R-squared:**	0.993
Model:	OLS	**Adj. R-squared:**	0.992
Method:	Least Squares	**F-statistic:**	3049.
Date:	Fri, 23 Nov 2018	**Prob (F-statistic):**	1.29e-49
Time:	16:13:18	**Log-Likelihood:**	226.91
No. Observations:	49	**AIC:**	-447.8
Df Residuals:	46	**BIC:**	-442.2

	coef	**std err**	**t**	**P>|t|**	**[95.0% Conf. Int.]**
Intercept	0.0004	0.001	0.423	0.674	-0.002 0.002
gammacc	0.0275	0.001	23.737	0.000	0.025 0.030
adhesion	0.3449	0.005	74.393	0.000	0.336 0.354

Omnibus:	6.291	**Durbin-Watson:**	0.991
Prob(Omnibus):	0.043	**Jarque-Bera (JB):**	6.036
Skew:	-0.859	**Prob(JB):**	0.0489
Kurtosis:	2.952	**Cond. No.**	15.6